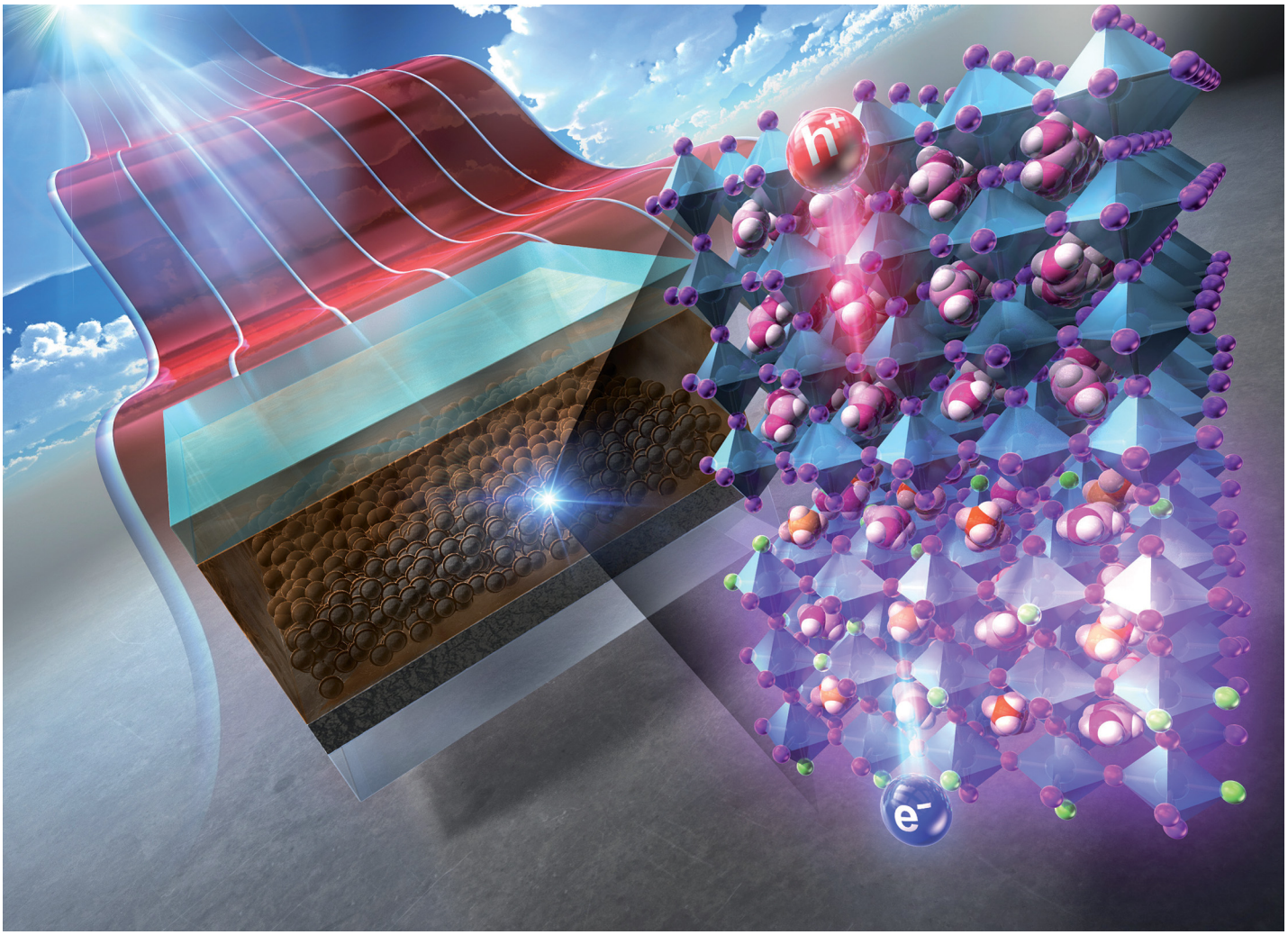

Showcasing research from National Institute of Advanced Industrial Science and Technology (AIST), Tsukuba, Japan.

Unveiled effects of the methylammonium chloride additive on formamidinium lead halide: expediting carrier injection from the photoabsorber to carrier transport layers through spontaneously modulated heterointerfaces in perovskite solar cells

Time-resolved spectroscopies unveil the additional effects of the widely used methylammonium chloride additive on $FAPbI_3$ photoabsorber in perovskite solar cells, spontaneously modulating heterointerfaces for accelerating carrier injections.

As featured in:

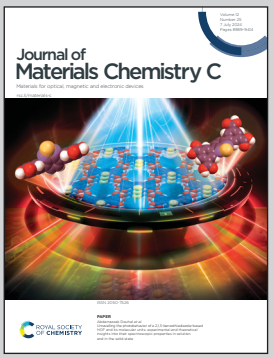

See Naoyuki Nishimura, Hiroyuki Matsuzaki *et al.*, *J. Mater. Chem. C*, 2024, **12**, 9130.

ROYAL SOCIETY OF CHEMISTRY

rsc.li/materials-c

Registered charity number: 207890

Journal of Materials Chemistry C

ROYAL SOCIETY OF CHEMISTRY

PAPER

View Article Online
View Journal | View Issue

Cite this: J. Mater. Chem. C, 2024, 12, 9130

Unveiled effects of the methylammonium chloride additive on formamidinium lead halide: expediting carrier injection from the photoabsorber to carrier transport layers through spontaneously modulated heterointerfaces in perovskite solar cells†

Naoyuki Nishimura, *[a] Ranjan Kumar Behera, [a] Ryuzi Katoh, [b] Hiroyuki Kanda, [a] Takurou N. Murakami [a] and Hiroyuki Matsuzaki *[a]

Received 2nd March 2024,
Accepted 28th May 2024

DOI: 10.1039/d4tc00843j

rsc.li/materials-c

Perovskite solar cells (PSCs) based on a narrow-bandgap formamidinium lead halide ($FAPbI_3$) photoabsorber have garnered substantial attention owing to their high photovoltaic (PV) performances. Extensive studies have established that the introduction of methylammonium chloride (MACl) significantly improves the quality of the $FAPbI_3$ bulk, and hence, this method has been commonly employed. Upon heating the photoabsorber's precursor film, the incorporated MACl facilitates the crystalline growth of $FAPbI_3$, simultaneously volatilizing and dissipating from the perovskite layer. However, not only the photoabsorber's bulk quality but also heterointerfaces between the photoabsorber and carrier transport materials importantly contribute to the PV performances. Paradoxically, the MACl effects on $FAPbI_3$ heterointerfaces have been sparingly explored and consequently remain elusive. Herein, the effects of MACl on these heterointerfaces are unveiled by time-resolved photoluminescence spectroscopy and time-resolved microwave conductivity. The MACl additive accelerates carrier injection from $FAPbI_3$ to the carrier transport materials presumably owing to the occurrence of spontaneous modulation of the heterointerfaces. In particular, at the heterointerface between $FAPbI_3$ and the titanium oxide (TiO_2) electron transport layer, an emissive interlayer, that is, a chloride-containing wide-bandgap $FA_{1-x}MA_xPbI_{3-y}Cl_y$ interlayer is formed spontaneously, which most likely has multiple advantages: hole blocking and facilitation of electron injection from $FAPbI_3$ to TiO_2 without additional hole trapping, leading to the observed PV performance enhancement. Consequently, the present results provide novel insights into the effects of the widely employed MACl additive on the $FAPbI_3$ photoabsorber, thereby propelling the further advancement of PSCs. Furthermore, this study demonstrates effective investigation of carrier dynamics with regard to the heterointerfaces, which is challenging, and will promote the development of the materials science field.

Introduction

Perovskite solar cells (PSCs) have been intensively studied as promising candidates for next-generation photovoltaic (PV) systems, owing to their potential for scalable production and high PV performances. This surge of interest in PSCs was triggered by the demonstration of a relatively high power conversion efficiency (PCE) approaching 10% for PSCs based on a methylammonium lead halide ($MAPbI_3$) photoabsorber in 2012.[1,2] Over the past decade, PSCs have undergone significant development by employing various techniques, including modifications to the composition of perovskite photoabsorbers, transitioning from the archetypal $MAPbI_3$ to A-site modulated perovskites.[3–11]

One of the most prominent compositions of perovskite photoabsorbers is formamidinium lead halide ($FAPbI_3$), distinguished by its narrow bandgap energy, relatively closely aligning with the ideal bandgap energy of single-junction PV ($\approx$1.4 eV).[5] Although $FAPbI_3$ was initially reported as a

[a] National Institute of Advanced Industrial Science and Technology (AIST), 1-1-1 Higashi, Tsukuba, Ibaraki 305-8565, Japan. E-mail: naoyuki-nishimura@aist.go.jp, hiroyuki-matsuzaki@aist.go.jp

[b] College of Engineering, Nihon University, Koriyama, Fukushima 963-8642, Japan

† Electronic supplementary information (ESI) available. See DOI: https://doi.org/10.1039/d4tc00843j

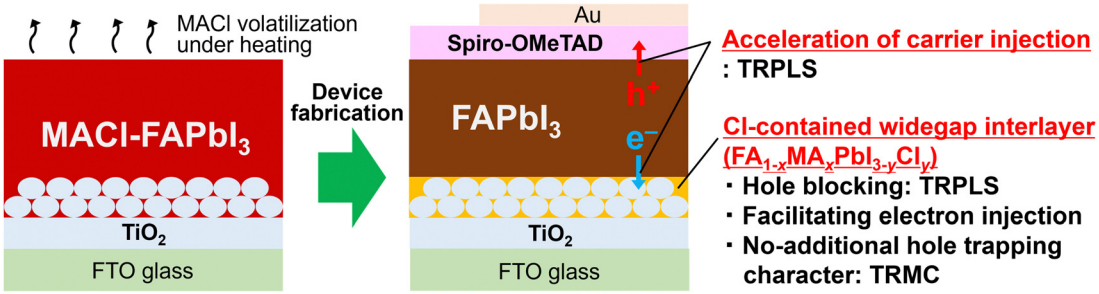

Fig. 1 Schematic illustration of unveiled effects of MACl: spontaneously modulated heterointerfaces facilitating carrier collection.

photoabsorber in the early stages of perovskite development in 2013,[5] challenges in film quality, pertaining to crystallinity and crystal phase control, impeded its progress. However, recent progress has successfully addressed this issue, establishing $FAPbI_3$ as a major photoabsorber.[5–27] Notably, the addition of alkylammonium chloride, typically methylammonium chloride (MACl), to the perovskite precursor has proven instrumental in achieving high-quality $FAPbI_3$ formation.[6–12] Upon heating the perovskite precursor film with the MACl additive, MACl facilitates crystal growth of $FAPbI_3$ and simultaneously volatilizes, contributing to improvements in film quality.[6–21] The MACl–$FAPbI_3$ system has become a widely acknowledged system, contributing to recent record-breaking PCE achievements.[11]

Meanwhile, PSCs consist of multiple layers (standard configuration from the top: metal conductor/hole transport material (HTM)/perovskite photoabsorber/electron transport material (ETM)/transparent conductor[1,2] (*e.g.*, Au/Spiro-OMeTAD/$FAPbI_3$/TiO_2/FTO: Fig. 1)). Consequently, PSC performance depends on the quality of the photoabsorber layer as well as on carrier injection from the photoabsorber to neighboring layers (*i.e.*, carrier transport layers). The manipulation of heterointerfaces, specifically the HTM/perovskite and perovskite/ETM interfaces, assumes a pivotal role in enhancing PV performances. Despite the established use of the MACl additive for improving $FAPbI_3$ bulk quality, the effects of MACl on heterointerfaces have been sparingly explored and consequently remain elusive. This is attributable to the inherent difficulty in differentiating MACl effects on the $FAPbI_3$ bulk from those on heterointerfaces. Thus, investigation of the nature of heterointerfaces independently of the bulk is imperative for the continued advancement of PSCs and the broader field of materials science.

This study elucidates the effects of the predominant MACl additive on carrier dynamics, specifically involving heterointerfaces in PSCs, employing time-resolved photoluminescence spectroscopy (TRPLS) and time-resolved microwave conductivity (TRMC). TRPLS measurements reveal two key features: (i) MACl addition accelerates carrier injection from $FAPbI_3$ to carrier transport layers and (ii) MACl induces the spontaneous formation of a chlorine (Cl)-containing wide-bandgap interlayer, $FA_{1-x}MA_xPbI_{3-y}Cl_y$, at the $FAPbI_3/TiO_2$ heterointerface. This $FA_{1-x}MA_xPbI_{3-y}Cl_y$ interlayer presumably functions as a hole-blocking layer and as an electron-injection facilitator. In addition, TRMC measurements indicate that the formed interlayer does not act as an additional hole trap, dispelling concerns about potential carrier trapping effects owing to the presence of the additional $FAPbI_3/FA_{1-x}MA_xPbI_{3-y}Cl_y$ heterointerface. In summary, this study reveals that MACl addition is advantageous not only for enhancing $FAPbI_3$ bulk quality but also for expediting carrier injection from $FAPbI_3$ to carrier transport materials through spontaneously modulated heterointerfaces (Fig. 1), thereby offering insights pivotal to the ongoing development of PSCs.

Results and discussion

Three distinct types of PSCs were fabricated, each based on different photoabsorbers: (i) MACl–$FAPbI_3$ with *n*-octylammonium iodide (OAI) passivation,[9,22,28–30] (ii) pristine MACl–$FAPbI_3$, and (iii) pristine $FAPbI_3$ without MACl. While the comparison between (i) and (ii) confirms the effects of OAI passivation, the comparative analysis between (ii) and (iii) reveals the effects of the MACl additive: not only the improvement of $FAPbI_3$ bulk quality but also the spontaneous modulation of the heterointerfaces in PSCs (Fig. 1).

Table 1 provides the PV parameters of the cells used in the subsequent TRPLS measurements. In the reverse scan, the PCEs were determined to be 20.9%, 16.9%, and 13.5% for cells based on MACl–$FAPbI_3$ with OAI passivation, pristine MACl–$FAPbI_3$, and pristine $FAPbI_3$ without MACl, respectively. Please refer to the ESI† for additional details, including statistical analysis of PV performance and other characterization methods.

This unequivocally confirms that the addition of MACl into $FAPbI_3$ substantially improved the PV performance,[6–9] with further enhancement observed with OAI passivation,[9,22] aligning with findings of previous reports. The X-ray diffraction (XRD) patterns (Fig. S4, ESI†) and the resultant larger grain size observed in the top view of scanning electron microscopy (SEM) images (Fig. S5, ESI†) suggest that the MACl addition

Table 1 PV performances of PSCs employed in TRPLS measurements

Sample	Scan	J_{sc} (mA cm^{-2})	V_{oc} (V)	FF	PCE (%)
OAI treated MACl–$FAPbI_3$	Reverse	25.5	1.12	0.73	20.9
	Forward	25.4	1.09	0.67	18.6
Pristine MACl–$FAPbI_3$	Reverse	24.1	0.97	0.73	16.9
	Forward	23.8	0.90	0.68	14.5
Pristine $FAPbI_3$ without MACl	Reverse	22.7	0.93	0.64	13.5
	Forward	22.6	0.90	0.54	11.1

likely improved the bulk quality[31,32] of $FAPbI_3$ with a little change in their bandgap energies: both have approximately 1.53 eV (Fig. S6, ESI†). Furthermore, TRMC measurement indicates enhancement of carrier mobility of $FAPbI_3$ when using the MACl additive (Fig. S7, ESI†). Consequently, the enhanced PV performance is attributed, in part, to the improved $FAPbI_3$ bulk, a phenomenon consistent with previous reports.[6–9] However, an additional contributing factor is the alteration of heterointerfaces pertinent to carrier collection, which will be discussed further.

To investigate the properties of the PSCs used in this study and to differentiate between bulk and heterointerface properties, TRPLS measurements were conducted. A comparative analysis between (i) the perovskite monolayer sample and (ii) the solar cell offers insights into the kinetics of carrier injection from the perovskite layer to the carrier transport materials. The PL lifetimes of (i) the perovskite monolayer samples serve as indicators of the carrier lifetime within each perovskite layer. The decay kinetics of the perovskite monolayer over the quartz substrate can be expressed by following relation:[33–35]

$$\frac{dn}{dt} = -An - Bn^2, \quad (1)$$

where n, A, and B represent the photoexcited carrier density, the rate constant of single-carrier trapping and/or recombination, and the rate constant of predominantly radiative bimolecular recombination, respectively. According to eqn (1), the PL lifetime depends on the photoexcited carrier density, which is adjustable by the excitation power. For instance, with weak excitation, the photoexcited carrier density (n) will be small, and so the first term (*i.e.*, $-An$) will primarily determine the PL lifetime. Meanwhile, with stronger excitation, the second term (*i.e.*, $-Bn^2$) will contribute more to the PL lifetime, leading to a steep decrease (Fig. S8, ESI†). Accordingly, fittings (Fig. 2 and Fig. S9, ESI†) following the PL lifetime measurements of the excitation power dependence (Fig. S8, ESI†) provide kinetic parameters A and B (see ESI† for more details). Consequently, the values of A and B, which primarily indicate $FAPbI_3$ bulk properties, are obtained by analyzing the excitation power dependence on the PL lifetime of (i) the $FAPbI_3$ monolayer samples.

Meanwhile, the extent of carrier decay in (ii) solar cells is expressed as follows:[33,34]

$$\frac{dn}{dt} = -An - Bn^2 - Cn \quad (2)$$

where C represents the total carrier-injection rate constant *via* heterointerfaces. Accordingly, utilizing the values of A and B obtained from (i) the monolayer perovskite samples, the fitting of the excitation power dependence on the PL lifetime of (ii) the solar cells (Fig. S10, ESI†) will provide the C values. For this fitting, the C values incorporate a time-dependent term[33] in this work. This is because actual carrier injection from perovskite to the carrier transport layers will cause carrier accumulation, and to express this feature, the C values should be time dependent. In more detail, carrier transport materials possess considerably lower mobility compared with perovskite materials (a difference exceeding three orders of magnitude). Thus, with strong excitation, carrier injection slows down at later times due to the accumulation of carriers at both the interfaces of the perovskite/carrier transport materials and within the bulk of the carrier transport materials. Therefore, C values necessitate a time-dependent term (see ESI† for more details.)

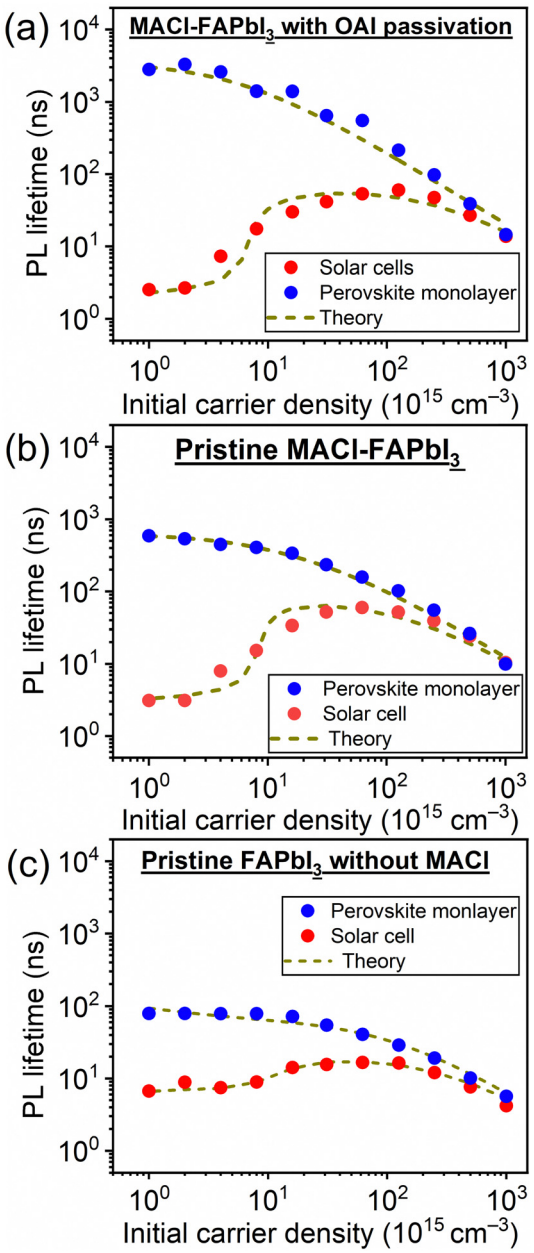

Fig. 2 Excitation power dependence of the PL lifetime of samples comprising (a) MACl–$FAPbI_3$ with OAI passivation, (b) pristine MACl–$FAPbI_3$, and (c) pristine $FAPbI_3$ without MACl additive.

These features based on eqn (1) and (2) were observed in the practical PL lifetime measurements, and the trends were different among the employed photoabsorber layers, indicating each carrier dynamics involving $FAPbI_3$ bulk quality and carrier injection from perovskite to carrier transport layers. Fig. 2

illustrates the excitation-power dependence of the PL lifetimes of both the solar cells and the corresponding perovskite monolayer on quartz substrate samples.[33–35] The PL lifetimes are defined as the time from the initial PL intensity to $1/e$ of that intensity, and the initial carrier densities per unit volume are calculated using excitation power densities per unit area and the absorption coefficient of $FAPbI_3$ at 650 nm[36] (see ESI† for more details). For the monolayer sample, when subjected to weak excitations, the dominance of single-carrier trapping and/or recombination (A) is evident, resulting in prolonged PL lifetimes, particularly in passivated samples, reaching the microsecond order. However, with stronger excitation, the contribution of bimolecular recombination (B) to carrier decay becomes more pronounced, consequently shortening the PL lifetime down to several nanoseconds.[33,34] In solar cells, carrier injection (C) is an additional factor contributing to carrier decay. Under weak excitation, carrier injection predominates, leading to a short PL lifetime within several nanoseconds. In contrast, stronger excitation slows down carrier injection due to the accumulation of carriers at both the interfaces of the perovskite/carrier transport materials and within the bulk of the carrier transport materials. As a result, moderate excitation power yields a longer PL lifetime compared to weak excitation. Ultimately, under further strong excitation, bimolecular recombination (B) becomes dominant, resulting in similar PL lifetime values for monolayer samples and solar cells under the strongest excitation (an initial carrier density of 10^{18} cm^{-3}).[33,34]

Moreover, the kinetics parameters were quantitatively determined by fitting the excitation power dependence of the PL lifetime[33,34] (see ESI† for fitting details). Table 2 presents the calculated kinetics parameters. According to eqn (1) and (2), smaller values of A and B indicate fewer carrier losses in the $FAPbI_3$ photoabsorber bulk, while a larger value of C represents faster carrier injection from $FAPbI_3$ to carrier-transport layers. A notable observation is the significant reduction of the A value by OAI passivation from 1.6×10^6 s^{-1} to 1.5×10^5 s^{-1} (a one-order decrease), while B and C values remain almost unchanged. This trend suggests that the primary role of OAI passivation is the suppression of defects inducing single-carrier trapping, thereby enhancing PV performance: an outcome consistent with prior reports.[9,22,28–30]

In contrast, a comparison between pristine MACl–$FAPbI_3$ and MACl-free $FAPbI_3$ samples showed trends different from those observed with/without OAI passivation, thereby revealing the effects of the MACl additive. The MACl addition not only reduced the A and B parameters, with A decreasing from 7.7×10^6 s^{-1} to 1.6×10^6 s^{-1} and B decreasing from 6.4×10^{-11} cm^3 s^{-1} to 3.5×10^{-11} cm^3 s^{-1}, indicating an improvement in $FAPbI_3$ bulk quality consistent with previous reports on MACl effects.[6–9] However, C values, pertaining to carrier injection, also underwent significant changes with MACl addition. The C value increased from 1.1×10^8 s^{-1} to 3.0×10^8 s^{-1} (an approximately three-fold increase), accelerating carrier injection from $FAPbI_3$ to carrier transport materials. This significant change in the C value strongly suggests that MACl addition not only affects the $FAPbI_3$ bulk but also influences the heterointerfaces between $FAPbI_3$ and carrier transport materials.

Table 2 Kinetics parameters of PSCs based on TRPLS

Sample	A (s^{-1})	B (cm^3 s^{-1})	C (s^{-1})
MACl–$FAPbI_3$ with OAI passivation	1.5×10^5	2.4×10^{-11}	2.5×10^8
Pristine MACl–$FAPbI_3$	1.6×10^6	3.5×10^{-11}	3.0×10^8
Pristine $FAPbI_3$ without MACl	7.7×10^6	6.4×10^{-11}	1.1×10^8

The PL spectra offer insights into changes at a heterointerface with the addition of MACl. Fig. 3 illustrates the time-resolved PL spectra of solar cells with and without MACl when excited from the FTO side. The PL spectra were segregated based on the time scale: the initial (0–5 ns) and the later part (30–50 ns). In the absence of MACl, minimal changes were observed in the PL spectra within the specified time range (Fig. 3a). On the contrary, for the sample with MACl, a notable spectral alteration emerged between the time intervals; a PL spectrum resembling that of the MACl-free counterpart, peaking at around 810 nm, was observed in the later time scale (30–50 ns), whereas in the initial time scale (0–5 ns), a blue-shifted PL was evident (Fig. 3b). The central photon energy of the deconvoluted blue-shifted PL was estimated to be 1.62 eV (765 nm; Fig. 3c), marking an approximately 90 meV increase compared with the primary PL (Fig. S11: 1.53 eV, 811 nm, ESI†). The absence of blue-shifted PL with excitation from the HTM side for the solar cell suggested its attribution to the ETM side (Fig. S12a, ESI†). Moreover, the sample of the MACl–$FAPbI_3$ perovskite monolayer on a quartz sample did not exhibit the blue-shifted PL (Fig. S12b, ESI†), leading to the conclusion that the observed short lifetime and blue-shifted PL originated from emission at the $FAPbI_3/TiO_2$ heterointerface, modulated by the presence of MACl.

The anticipated modulation of the $FAPbI_3/TiO_2$ heterointerface and the resulting blue-shifted PL observed in Fig. 3c, attributed to the Cl composition derived from MACl, prompted a comprehensive compositional depth analysis. Secondary ion mass spectroscopy (SIMS) results depicted in Fig. 4 showcase $FAPbI_3$ with and without MACl samples using TiO_2/FTO substrates, distinguished by the presence of Pb and I, Ti, and Sn for $FAPbI_3$, TiO_2, and FTO, respectively. In the MACl-containing sample, a significantly heightened Cl intensity exceeding 1000 counts was observed in the TiO_2 region, approximately ten-fold higher than that in the perovskite regime. This observation unequivocally indicates the segregation of Cl from MACl at the $FAPbI_3/TiO_2$ heterointerface, forming a Cl-containing interlayer, presumed to be $FAPbI_{3-y}Cl_y$.

Considering the bandgaps of $MAPbCl_3$ (3.11 eV)[37,38] and $FAPbI_3$ (1.53 eV; Fig. S6 and S11, ESI†), and a linear bandgap relation between them was premised, 5 mol% Cl composition in the perovskite halogen (*i.e.*, $FAPbI_{2.85}Cl_{0.15}$) could be roughly estimated, based on the blue-shifted PL energy of 1.62 eV, as observed in Fig. 3c. The estimated Cl content of 5 mol% may be high with respect to the FA cation in the A-site of the perovskite regarding crystal structure distortion. Therefore, a small portion of MA cations from MACl can be contained in the $FAPbI_{3-y}Cl_y$ interlayer ($FA_{1-x}MA_xPbI_{3-y}Cl_y$), thus mitigating

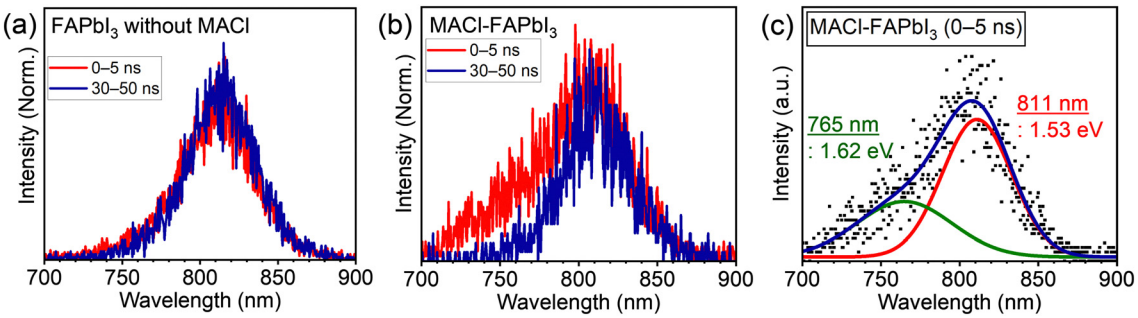

Fig. 3 PL spectra of solar cells consisting of (a) $FAPbI_3$ without MACl and (b) the MACl–$FAPbI_3$ photoabsorber divided by time scales of 0–5 ns and 30–50 ns. (c) Deconvoluted spectra of the MACl–$FAPbI_3$ cell in the initial time scale (0–5 ns).

crystal distortion.[8,10] Consequently, owing to the high Cl content at the $FAPbI_3/TiO_2$ interface, the observed blue-shifted PL shown in Fig. 3c is most likely attributed to the spontaneously formed $FA_{1-x}MA_xPbI_{3-y}Cl_y$ interlayer.

Furthermore, the depth of the high-Cl-regime correlated well with the high-Ti region on the measured scale, suggesting a thin thickness for the $FA_{1-x}MA_xPbI_{3-y}Cl_y$ interlayer. This assumed thin thickness implies that a robust chemical interaction between the Cl^- anion and the TiO_2 surface induced the formation of the $FA_{1-x}MA_xPbI_{3-y}Cl_y$ interlayer, likely not limited by the diffusion of Cl^- anions in the perovskite precursor film. In other words, the relatively distant position of the Cl^- contained interlayer from the gas phase, which is unfavorable for volatilization, is unlikely the primary reason for interlayer formation. Instead, the chemical interaction between Cl^- and TiO_2 is presumed to be the primary factor contributing to the formation of the $FA_{1-x}MA_xPbI_{3-y}Cl_y$ interlayer. Hence, this spontaneous modulation of the perovskite/TiO_2 interface with the Cl content derived from MACl would occur for both the mesoporous TiO_2 ETMs and planar TiO_2 ETMs,[39–43] taking advantage of the chemical interaction.

Even for the sample without MACl, a detectable Cl signal, up to 50 counts, was observed in the TiO_2 region (Fig. 4b). This weak Cl signal originates from the m-TiO_2 utilized in this study, as confirmed by SIMS measurements on a TiO_2/FTO reference sample (Fig. S13, ESI†). This implies a trace amount of Cl contamination in the production process of m-TiO_2. Although the employed m-TiO_2 does contain some Cl, the quantity is significantly lower (over 200 times less) than that of the spontaneously formed $FA_{1-x}MA_xPbI_{3-y}Cl_y$ interlayer (Fig. 4). Hence, the presence of Cl in m-TiO_2 negligibly influences the PV performance of samples without MACl.

The presence of $FA_{1-x}MA_xPbI_{3-y}Cl_y$ is deemed advantageous for carrier collection, attributed to two key aspects: (i) its nature as a hole-blocking layer and (ii) the strong interfacial coupling between TiO_2 and $FA_{1-x}MA_xPbI_{3-y}Cl_y$, facilitating efficient electron injection. The (i) hole-blocking nature is based on the assumption of energy alignment within the wide-bandgap interlayer (Fig. 5). Since halogen anions contribute more to the valence band (VB) of the perovskite than the conduction band (CB),[44] the formed $FA_{1-x}MA_xPbI_{3-y}Cl_y$ interlayer likely possesses a deeper VB top compared to $FAPbI_3$, with a marginal change in the CB bottom energy. The short PL lifetime of the $FA_{1-x}MA_xPbI_{3-y}Cl_y$ interlayer indicates rapid hole transfer from $FA_{1-x}MA_xPbI_{3-y}Cl_y$ to $FAPbI_3$. This short lifetime also implies that holes cannot access the $FA_{1-x}MA_xPbI_{3-y}Cl_y$ interlayer from $FAPbI_3$ (*i.e.*, hole transfer from $FAPbI_3$ to the $FA_{1-x}MA_xPbI_{3-y}Cl_y$ interlayer cannot proceed), as PL occurs only when both electrons and holes coexist in a material. This hole-blocking feature aligns with the assumed energy gap of VB tops between $FAPbI_3$ and $FA_{1-x}MA_xPbI_{3-y}Cl_y$, differing by up to 90 meV, a substantial difference from room temperature energy ($kT \approx 26$ meV). Therefore, the wide-bandgap $FA_{1-x}MA_xPbI_{3-y}Cl_y$ interlayer likely functioned as a hole-blocking layer, contributing favorably to charge separation (Fig. 5). We here

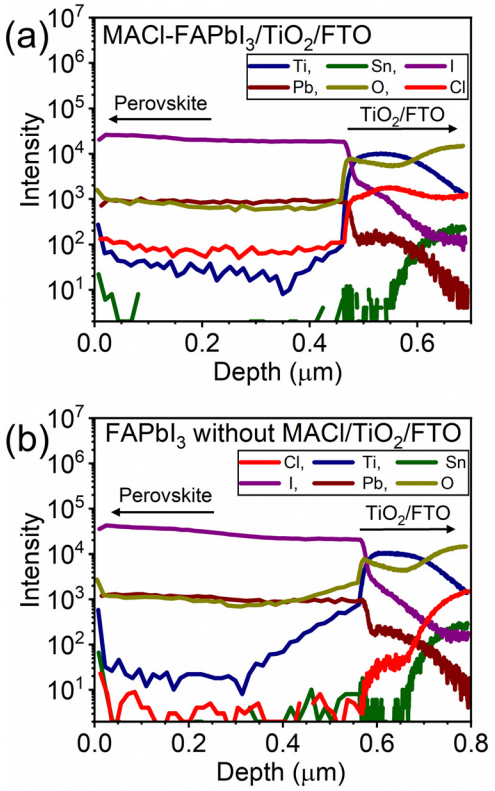

Fig. 4 Compositional depth analysis of (a) MACl–$FAPbI_3/TiO_2$/FTO and (b) $FAPbI_3$ without MACl/TiO_2/FTO.

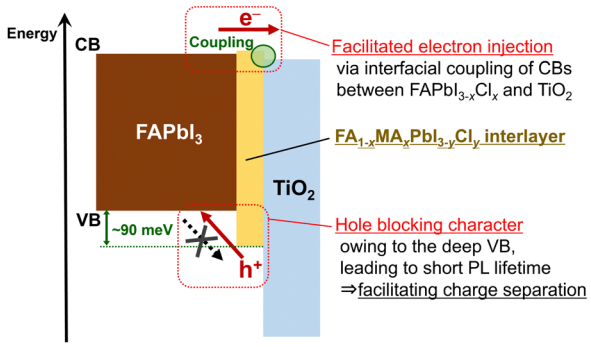

Fig. 5 Illustration of the functions of the wide-bandgap $FA_{1-x}MA_xPbI_{3-y}Cl_y$ interlayer formed between $FAPbI_3$ and TiO_2.

note that the hole leaking from $FAPbI_3$ to FTO potentially occurs *via* physical pinholes in the TiO_2 layer[45–51] and/or *via* defect states in TiO_2 shallower than the VB top of TiO_2.[39,52,53] Therefore, the presence of the $FA_{1-x}MA_xPbI_{3-y}Cl_y$ interlayer possessing the VB deeper than $FAPbI_3$ is advantageous for blocking the hole leaking regardless of the deeper VB top of TiO_2 than that of $FAPbI_3$.

Regarding (ii) the strong interfacial coupling, certain density functional theory calculations indicate that interfacial Cl in perovskites results in robust electron coupling and chemical bonding to TiO_2.[54,55] Specifically, the partial density of states calculations illustrate that Cl incorporation into a perovskite material strengthens the interfacial coupling of CBs between the unoccupied titanium d-orbital in TiO_2 and the lead p-orbital in a perovskite.[54] Enhanced CB coupling is advantageous for more efficient electron injection (Fig. 5). Consequently, the formed $FA_{1-x}MA_xPbI_{3-y}Cl_y$ interlayer likely contributes to the accelerated carrier collection observed in Fig. 2.

The potential concern that the introduction of an additional heterointerface might act as a carrier trap led to an investigation into the carrier-trap nature of the Cl-contained $FAPbI_3$/TiO_2 interlayer by TRMC.[23,56–62] We have recently proposed TRMC as an effective means to probe the carrier-trap nature of heterointerfaces in PSCs.[23] After carrier injection from the perovskite to a carrier transport material, TRMC detects the lifetime of the remaining carriers in the perovskite, considering that the carrier mobility of carrier transport materials is negligible compared to perovskite materials[23,59] (see ESI† for details). Fig. 6 illustrates TRMC signal decays of the MACl–$FAPbI_3$ monolayer on a quartz sample and the $FAPbI_3$–MACl/TiO_2 bilayer on a quartz sample. Here, we note that for the excitation conditions shown in Fig. 6, weak excitation power, where bimolecular recombination (B in eqn 1) becomes negligible and single-carrier trapping and/or recombination (A in eqn 1) dominates the carrier lifetime, was employed (see Fig. S14; excitation power dependence of TRMC decays, ESI†). In the short time scale of the TRMC signal shown in Fig. S15 (ESI†), the MACl–$FAPbI_3$/TiO_2 bilayer sample exhibited a steep decay corresponding to electron injection from perovskite to TiO_2 in the early stage, but the monolayer sample did not. In light of this electron injection, consequently, single and double exponential fittings were employed for the analysis of the long-time range TRMC decay for the monolayer and bilayer samples, respectively (Fig. 6b and c). Table 3 details each lifetime based on the fitting.

Table 3 TRMC signal lifetimes

Sample	τ_1 (μs)	τ_2 (μs)	$\tau_{average}$ (μs)
MACl–$FAPbI_3$ monolayer	50 ± 1	—	50 ± 1
MACl–$FAPbI_3$/TiO_2 bilayer	2.7 ± 1.1	62 ± 7	57 ± 2

The MACl–$FAPbI_3$ monolayer sample exhibited a lifetime (τ) of 50 ± 1 μs. Meanwhile, the MACl–$FAPbI_3$/TiO_2 bilayer sample showed a short lifetime (τ_1) of 2.7 ± 1.1 μs and a long lifetime (τ_2) of 62 ± 7 μs, resulting in an average lifetime ($\tau_{average}$) of 57 ± 2 μs with each component weight in the fitting of A_1 = 0.08 and A_2 = 0.92. The longer lifetime of the τ_2 component of the bilayer sample relative to the monolayer lifetime τ implies that the $FA_{1-x}MA_xPbI_{3-y}Cl_y$ interlayer might suppress hole traps over TiO_2. However, the similar values of average lifetimes of the monolayer and bilayer samples indicate that the $FA_{1-x}MA_xPbI_{3-y}Cl_y$ interlayer does not act as an additional hole trap (Fig. 6d). Consequently, the spontaneously formed $FA_{1-x}MA_xPbI_{3-y}Cl_y$ interlayer with the MACl additive is not detrimental to the hole lifetime; yet, it likely facilitates carrier collection.

Conclusions

In this study, the effects of MACl, a widely employed additive for a narrow-bandgap $FAPbI_3$ photoabsorber, are unveiled through the application of time-resolved spectroscopies for investigating carrier dynamics of PSCs. While the MACl additive is recognized for its role in enhancing $FAPbI_3$ bulk quality, our investigation, employing the excitation power dependence

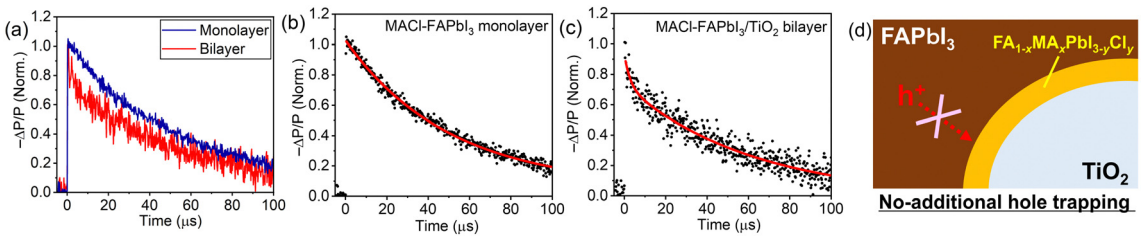

Fig. 6 (a) TRMC signal decays of the MACl–$FAPbI_3$ monolayer and MACl–$FAPbI_3$/TiO_2 bilayer samples; fitting curves for the (b) monolayer sample and (c) bilayer sample; and (d) illustration of no-additional hole-trapping nature of the $FA_{1-x}MA_xPbI_{3-y}Cl_y$ interlayer.

of TRPLS, has unveiled its additional effectiveness in expediting carrier injection from $FAPbI_3$ to carrier transport materials. (Fig. 1)

Furthermore, through a combination of TRPLS and compositional depth analysis (SIMS), it was observed that the MACl additive results in the formation of a Cl-containing wide-bandgap interlayer ($FA_{1-x}MA_xPbI_{3-y}Cl_y$: $\approx$1.62 eV) at the $FAPbI_3/TiO_2$ interface, with a short lifetime of several nanoseconds. The $FA_{1-x}MA_xPbI_{3-y}Cl_y$ interlayer is proposed to serve two key functions: (i) acting as a hole-blocking layer advantageous for charge separation due to its deep VB top and (ii) facilitating electron injection from $FAPbI_3$ to TiO_2 owing to the strong interfacial coupling between their CBs. (Fig. 5) The TRMC measurements indicate that the formed $FA_{1-x}MA_xPbI_{3-y}Cl_y$ interlayer does not exhibit additional hole-trapping characteristics (Fig. 6c), suggesting that it is not detrimental to the PV performances rather presumably accelerating carrier collection (Fig. 1).

In conclusion, our findings demonstrate that the MACl additive, beyond its role in improving $FAPbI_3$ bulk quality, spontaneously modulates heterointerfaces and accelerates carrier injection from $FAPbI_3$ to carrier transport materials. This work provides valuable insights into the effects of the commonly used MACl additive on a promising $FAPbI_3$ photoabsorber, contributing to the ongoing development of PSCs. Furthermore, the effective investigation of heterointerfaces performed in this study using time-resolved spectroscopies serves as a crucial demonstration, paving the way for the development of an effective means to explore multi-layered devices for solar energy conversion, including solar PV systems, and contributing to the advancement of the broad field of materials science.

Experimental section

Solar cell fabrication

PSC fabrication was achieved by following conventional methods with minor adjustments,[22,23] as detailed in the ESI.† Initially, mesoporous TiO_2 (m-TiO_2)/compact layer TiO_2 (c-TiO_2)/FTO substrates were prepared using spray pyrolysis for c-TiO_2 and spin-coating for m-TiO_2. Subsequently, the $FAPbI_3$ perovskite layer was deposited on the TiO_2/FTO substrates by spin-coating in a dry air atmosphere. The $FAPbI_3$ precursor solution, comprising synthesized $FAPbI_3$ powder (with 40 mol% MACl for the $FAPbI_3$ powder), was prepared by dissolving it in a mixed solution of *N*,*N*-dimethylformamide and dimethyl sulfoxide. The substrate was spin-coated with the precursor solution at 6000 rpm for 50 s and promptly heated at 423 K for 10 min. During the spin-coating process, 1 mL of chlorobenzene was introduced after spinning for 10 s. In certain samples, OAI passivation over the as-prepared $FAPbI_3$ layer was implemented to suppress perovskite surface defects. This involved spin-coating an OAI/isopropyl alcohol solution over the $FAPbI_3$ layer, followed by heating at 373 K for 5 min. The deposition of the HTM was accomplished through spin-coating a solution containing Spiro-OMeTAD and additives. Finally, a 200 nm thick Au conductor layer was deposited *via* thermal evaporation.

PV performance measurement

Current–voltage curves were systematically acquired using a source meter (R6243, ADVANTEST) and a solar simulator (XIL-05B100KP, Seric Co.), calibrated with a Si-reference cell to generate AM1.5G illumination (100 mW cm^{-2}). The current–voltage scans were conducted at a constant speed of 100 mV s^{-1}, concurrently exposed to simulated sunlight. Each experimental condition encompassed measurements on over 10 samples, from which the most optimal specimens were selected. Subsequently, the solar cell properties were computed based on the averages with standard deviations derived from the chosen samples.

TRPLS measurements

TRPLS measurements[35] were conducted on the solar cells and perovskite quartz monolayer samples prepared utilizing the same methodology that was employed for the solar cells using a streak camera (Hamamatsu Photonics, StreakScope C4334) equipped with a monochromator. A Ti:sapphire laser with a regenerative amplifier (Spectra-Physics, Solstice; a central wavelength of 800 nm, a pulse width of 100 fs, a pulse energy of 3.5 mJ per pulse, and a repetition rate of 1 kHz) was used as a light source. Part of the output from the laser was used for the excitation of an optical parametric amplifier (OPA; Spectra-Physics, TOPAS Prime). The output from the OPA at a wavelength of 650 nm was used as the excitation light, unless stated otherwise. The samples were excited from the glass side. The excitation light was filtered with a long-pass color glass filter ($>$700 nm, R70) and only the PL from the sample was detected by the measurement apparatus. The irradiated area of the excitation light at the sample position was evaluated using a beam profiler (Newport LBP2-HR-VIS2). All the measurements were conducted in air at room temperature ($\sim$297 K).

TRMC measurements

TRMC measurements for MACl–$FAPbI_3$ on a quartz monolayer sample and MACl–$FAPbI_3/TiO_2$ on a quartz bilayer sample were executed within custom-designed apparatus. Both samples were subjected to OAI passivation. The excitation source employed was the second harmonic (532 nm) of a Nd^{3+}:YAG laser (VN-200-10-ST, VM-TIM). Further details regarding the experimental configuration can be found elsewhere.[56,58]

Author contributions

Naoyuki Nishimura: conceptualization, project administration, investigation, resources, formal analysis, writing – original draft, writing – reviewing and editing; Ranjan Kumar Behera: formal analysis, investigation, writing – reviewing and editing; Ryuzi Katoh: investigation, writing – reviewing and editing; Hiroyuki Kanda: writing – reviewing and editing; Takurou N.

Murakami: funding acquisition, writing – reviewing and editing; and Hiroyuki Matsuzaki: investigation, formal analysis, conceptualization, project administration, supervision, writing – reviewing and editing.

Conflicts of interest

There are no conflicts to declare.

Acknowledgements

This article is based on results obtained from a project, JPNP21016, commissioned by the New Energy and Industrial Technology Development Organization (NEDO).

References

1 M. M. Lee, J. Teuscher, T. Miyasaka, T. N. Murakami and H. J. Snaith, *Science*, 2012, **338**, 643–647.
2 H. S. Kim, C. R. Lee, J. H. Im, K. B. Lee, T. Moehl, A. Marchioro, S. J. Moon, R. Humphry-Baker, J. H. Yum, J. E. Moser, M. Gratzel and N. G. Park, *Sci. Rep.*, 2012, **2**, 591.
3 M. Saliba, T. Matsui, J. Y. Seo, K. Domanski, J. P. Correa-Baena, M. K. Nazeeruddin, S. M. Zakeeruddin, W. Tress, A. Abate, A. Hagfeldt and M. Gratzel, *Energy Env. Sci.*, 2016, **9**, 1989–1997.
4 M. Saliba, T. Matsui, K. Domanski, J. Y. Seo, A. Ummadisingu, S. M. Zakeeruddin, J. P. Correa-Baena, W. R. Tress, A. Abate, A. Hagfeldt and M. Gratzel, *Science*, 2016, **354**, 206–209.
5 T. M. Koh, K. Fu, Y. Fang, S. Chen, T. C. Sum, N. Mathews, S. G. Mhaisalkar, P. P. Boix and T. Baikie, *J. Phys. Chem. C*, 2013, **118**, 16458–16462.
6 Z. Wang, Y. Zhou, S. Pang, Z. Xiao, J. Zhang, W. Chai, H. Xu, Z. Liu, N. P. Padture and G. Cui, *Chem. Mater.*, 2015, **27**, 7149–7155.
7 F. Xie, C.-C. Chen, Y. Wu, X. Li, M. Cai, X. Liu, X. Yang and L. Han, *Energy Env. Sci.*, 2017, **10**, 1942–1949.
8 M. Kim, G.-H. Kim, T. K. Lee, I. W. Choi, H. W. Choi, Y. Jo, Y. J. Yoon, J. W. Kim, J. Lee, D. Huh, H. Lee, S. K. Kwak, J. Y. Kim and D. S. Kim, *Joule*, 2019, **3**, 2179–2192.
9 J. Jeong, M. Kim, J. Seo, H. Lu, P. Ahlawat, A. Mishra, Y. Yang, M. A. Hope, F. T. Eickemeyer, M. Kim, Y. J. Yoon, I. W. Choi, B. P. Darwich, S. J. Choi, Y. Jo, J. H. Lee, B. Walker, S. M. Zakeeruddin, L. Emsley, U. Rothlisberger, A. Hagfeldt, D. S. Kim, M. Gratzel and J. Y. Kim, *Nature*, 2021, **592**, 381–385.
10 L. Bi, Q. Fu, Z. Zeng, Y. Wang, F. R. Lin, Y. Cheng, H. L. Yip, S. W. Tsang and A. K. Jen, *J. Am. Chem. Soc.*, 2023, **145**, 5920–5929.
11 J. Park, J. Kim, H. S. Yun, M. J. Paik, E. Noh, H. J. Mun, M. G. Kim, T. J. Shin and S. I. Seok, *Nature*, 2023, **616**, 724–730.
12 H. Min, M. Kim, S. U. Lee, H. Kim, G. Kim, K. Choi, J. H. Lee and S. I. Seok, *Science*, 2019, **366**, 749–753.
13 E. Choi, J. W. Lee, M. Anaya, A. Mirabelli, H. Shim, J. Strzalka, J. Lim, S. Yun, M. Dubajic, J. Lim, J. Seidel, R. E. Agbenyeke, C. G. Kim, N. J. Jeon, A. M. Soufiani, H. H. Park and J. S. Yun, *Adv. Ener. Mater.*, 2023, **13**, 2301717.
14 K. A. Elmestekawy, B. M. Gallant, A. D. Wright, P. Holzhey, N. K. Noel, M. B. Johnston, H. J. Snaith and L. M. Herz, *ACS Energy Lett.*, 2023, **8**, 2543–2551.
15 X. Huang, F. Cao, S. Zhan, Q. Feng, M. Zhu, Z. Su, X. Gao, J. Yin, J. Li, N. Zheng and B. Wu, *Joule*, 2023, **7**, 1556–1573.
16 Y. Kim, G. Kim, E. Y. Park, C. S. Moon, S. J. Lee, J. J. Yoo, S. Nam, J. Im, S. S. Shin, N. J. Jeon and J. Seo, *Energy Env. Sci.*, 2023, **16**, 2226–2238.
17 S. Ryu, B. Gil, B. Kim, J. Kim and B. Park, *ACS Appl. Mater. Interfaces*, 2023, **15**(49), 56909–56917.
18 D. Dastan, M. K. A. Mohammed, R. Sh Alnayli, S. M. Majeed, D. S. Ahmed, A. K. Al-Mousoi, R. Pandey, M. K. Hossain, S. Bhattarai, B. A. Al-Asbahi and M. F. Rahman, *Langmuir*, 2024, **40**, 7560–7568.
19 J. Ge, R. Chen, Y. Ma, Y. Wang, Y. Hu, L. Zhang, F. Li, X. Ma, S. W. Tsang, J. You, A. K. Y. Jen and S. F. Liu, *Angew. Chem., Int. Ed.*, 2024, **63**, e202319282.
20 K. Park, S. Tan, T. Kodalle, D. K. Lee, M. Abdelsamie, J. S. Park, J. H. Lee, S. K. Jung, J. H. Ko, N. G. Park, C. M. Sutter-Fella, Y. Yang and J. W. Lee, *Adv. Mater.*, 2024, **36**, e2307265.
21 X. Wang, H. Huang, M. Wang, Z. Lan, P. Cui, S. Du, Y. Yang, L. Yan, Q. Zhang, S. Qu and M. Li, *Adv. Mater.*, 2024, **36**, e2310710.
22 N. Nishimura, S. Mathew and T. N. Murakami, *New J. Chem.*, 2023, **47**, 4197–4201.
23 N. Nishimura, H. Tachibana, R. Katoh, H. Kanda and T. N. Murakami, *ACS Appl. Mater. Interfaces*, 2023, **15**, 44859–44866.
24 J. W. Yoo, E. Noh, J. Jang, K. S. Lee, J. Byeon, M. Choi, J. Im and S. I. Seok, *Joule*, 2023, **7**, 797–809.
25 K. Huang, L. Chang, Y. Hou, W. Ji, T. Trân-Phú, A. D. Bui, A. O. Mayon, W. Wang, O. L. C. Lem, D. T. Nguyen, G. D. Tabi, L. Duan, Y. Liu, H. Shen, J. Yang, T. P. White, K. R. Catchpole, K. J. Weber and T. Duong, *Adv. Ener. Mater.*, 2024, 2304073.
26 Y. Wang, S.-C. Chen, S. Tai, D. Wang, Y. Ma, J. Wu and M.-J. Lin, *J. Mater. Chem. C*, 2024, **12**, 6540–6547.
27 F. Feng, Y. Guan, F. Liu, C. Wu, H. Su, B. Wang, X. Zhang, Y. Liang, S. Cai, Y. Zhang, L. Xiao and S. Zheng, *J. Mater. Chem. C*, 2024, **12**, 3410–3417.
28 T. M. Koh, V. Shanmugam, X. Guo, S. S. Lim, O. Filonik, E. M. Herzig, P. Müller-Buschbaum, V. Swamy, S. T. Chien, S. G. Mhaisalkar and N. Mathews, *J. Mater. Chem. A*, 2018, **6**, 2122–2128.
29 H. Kim, S. U. Lee, D. Y. Lee, M. J. Paik, H. Na, J. Lee and S. I. Seok, *Adv. Energy Mater.*, 2019, **9**, 1902740.
30 S. Akin, B. Dong, L. Pfeifer, Y. Liu, M. Graetzel and A. Hagfeldt, *Adv. Sci.*, 2021, **8**, 2004593.
31 J. Y. Chun, B. G. Kim, W. Jang and D. H. Wang, *Appl. Surf. Sci.*, 2022, **591**, 22.153207.

32 W. Jang, J. Lee, B. G. Kim, J. Lim, Z. Yang and D. H. Wang, *Cryst. Growth Des.*, 2023, **23**, 6916–6925.
33 T. Handa, D. M. Tex, A. Shimazaki, A. Wakamiya and Y. Kanemitsu, *J. Phys. Chem. Lett.*, 2017, **8**, 954–960.
34 Y. Kanemitsu and T. Handa, *Jpn. J. Appl. Phys.*, 2018, **57**, 090101.
35 Y. Pihosh, V. Nandal, R. Shoji, R. Bekarevich, T. Higashi, V. Nicolosi, H. Matsuzaki, K. Seki and K. Domen, *ACS Energy Lett.*, 2023, **8**, 2106–2112.
36 A. D. Wright, G. Volonakis, J. Borchert, C. L. Davies, F. Giustino, M. B. Johnston and L. M. Herz, *Nat. Mater.*, 2020, **19**, 1201–1206.
37 G. C. Papavassiliou and I. B. Koutselas, *Synth. Met.*, 1995, **71**, 1713–1714.
38 N. Kitazawa, Y. Watanabe and Y. Nakamura, *J. Mater. Sci.*, 2002, **37**, 3585–3587.
39 H. Tan, A. Jain, O. Voznyy, X. Lan, F. P. Garcia de Arquer, J. Z. Fan, R. Quintero-Bermudez, M. Yuan, B. Zhang, Y. Zhao, F. Fan, P. Li, L. N. Quan, Y. Zhao, Z. H. Lu, Z. Yang, S. Hoogland and E. H. Sargent, *Science*, 2017, **355**, 722–726.
40 E. Mosconi, E. Ronca and F. De Angelis, *J. Phys. Chem. Lett.*, 2014, **5**, 2619–2625.
41 Y. Ding, B. Ding, H. Kanda, O. J. Usiobo, T. Gallet, Z. Yang, Y. Liu, H. Huang, J. Sheng, C. Liu, Y. Yang, V. I. E. Queloz, X. Zhang, J. N. Audinot, A. Redinger, W. Dang, E. Mosconic, W. Luo, F. De Angelis, M. Wang, P. Dorflinger, M. Armer, V. Schmid, R. Wang, K. G. Brooks, J. Wu, V. Dyakonov, G. Yang, S. Dai, P. J. Dyson and M. K. Nazeeruddin, *Nat. Nanotechnol.*, 2022, **17**, 598–605.
42 N. Lalpour, V. Mirkhani, R. Keshavarzi, M. Moghadam, S. Tangestaninejad, I. Mohammadpoor-Baltork and P. Gao, *Sci. Rep.*, 2023, **13**, 6368.
43 J. Liu, S. Li, Z. Qiu, Y. Liu, C. Qiu, W. Zhang, J. Qi, K. Chen, W. Wang, C. Wang, Z. Cui, Y. Su, Y. Hu, A. Mei and H. Han, *Small*, 2023, **19**, e2300737.
44 X. Pu, Q. Cao, J. Su, J. Yang, T. Wang, Y. Zhang, H. Chen, X. He, X. Chen and X. Li, *Adv. Energy Mater.*, 2023, **13**, 2301607.
45 S. Takahashi, S. Uchida, P. V. V. Jayaweera, S. Kaneko and H. Segawa, *Sci. Rep.*, 2023, **13**, 16068.
46 G. Giorgi, J. Fujisawa, H. Segawa and K. Yamashita, *J. Phys. Chem. Lett.*, 2013, **4**, 4213–4216.
47 Y. Wu, X. Yang, H. Chen, K. Zhang, C. Qin, J. Liu, W. Peng, A. Islam, E. Bi, F. Ye, M. Yin, P. Zhang and L. Han, *Appl. Phys. Express*, 2014, **7**, 052301.
48 J. Choi, S. Song, M. T. Horantner, H. J. Snaith and T. Park, *ACS Nano*, 2016, **10**, 6029–6036.
49 C. H. Ji, K. T. Kim and S. Y. Oh, *RSC Adv.*, 2018, **8**, 8302–8309.
50 X. Guo, B. Zhang, Z. Lin, J. Ma, J. Su, W. Zhu, C. Zhang, J. Zhang, J. Chang and Y. Hao, *Org. Electron.*, 2018, **62**, 459–467.
51 M. T. Masood, S. Qudsia, M. Hadadian, C. Weinberger, M. Nyman, C. Ahlang, S. Dahlstrom, M. Liu, P. Vivo, R. Osterbacka and J. H. Smatt, *Nanomaterials*, 2020, **10**, 10010181.
52 S. Sandhu, C. Saharan, S. K. Buruga, S. A. Kumar, P. S. Rana, P. C. Nagajyothi and S. D. Mane, *Ceram. Int.*, 2021, **47**, 14665–14672.
53 Z. Dong, J. Wang, J. Men, J. Zhang, J. Wu, Y. Lin, X. Xie, J. Wang and J. Zhang, *Inorg. Chem.*, 2024, **63**, 5709–5717.
54 K.-M. Lee, W.-J. Lin, S.-H. Chen and M.-C. Wu, *Org. Electron.*, 2020, **77**, 105406.
55 S.-H. Chen, C.-M. Ho, Y.-H. Chang, K.-M. Lee and M.-C. Wu, *Chem. Eng. J.*, 2022, **445**, 136761.
56 R. Katoh, A. Furube, K.-i Yamanaka and T. Morikawa, *J. Phys. Chem. Lett*, 2010, **1**, 3261–3265.
57 H. Oga, A. Saeki, Y. Ogomi, S. Hayase and S. Seki, *J. Am. Chem. Soc.*, 2014, **136**, 13818–13825.
58 S. Nakajima and R. Katoh, *J. Mater. Chem. A*, 2015, **3**, 15466–15472.
59 E. M. Hutter, J. J. Hofman, M. L. Petrus, M. Moes, R. D. Abellón, P. Docampo and T. J. Savenije, *Adv. Energy Mater.*, 2017, **7**, 1602349.
60 M. L. Petrus, K. Schutt, M. T. Sirtl, E. M. Hutter, A. C. Closs, J. M. Ball, J. C. Bijleveld, A. Petrozza, T. Bein, T. J. Dingemans, T. J. Savenije, H. Snaith and P. Docampo, *Adv. Energy Mater.*, 2018, **8**, 1801605.
61 N. Nishimura, H. Kanda, R. Katoh, A. Kogo and T. N. Murakami, *J. Mater. Chem. A*, 2024, DOI: **10.1039/D4TA02036G**.
62 N. Nishimura, H. Tachibana, R. Katoh, H. Kanda and T. N. Murakami, *ChemRxiv*, 2024, DOI: **10.26434/chemrxiv-2024-ts5k7**.

